

The effect of microstructure and film composition on the mechanical properties of linear antenna CVD diamond thin films

Rani Mary Joy^{a,b,1}, Paulius Pobedinskas^{a,b,1}, Nina Baule^c, Shengyuan Bai^d, Daen Jannis^{e,f}, Nicolas Gauquelin^{e,f}, Marie-Amandine Pinault-Thaury^g, François Jomard^g, Kamatchi Jothiramalingam Sankaran^{a,b,2}, Rozita Rouzbahani^{a,b}, Fernando Lloret^{a,b,3}, Derese Desta^{a,b}, Jan D'Haen^{a,b}, Johan Verbeeck^{e,f}, Michael Frank Becker^c, Ken Haenen^{a,b}

^a*Institute for Materials Research (IMO), Hasselt University, Wetenschapspark 1, B-3590 Diepenbeek, Belgium*

^b*IMOMECA, IMEC vzw, Wetenschapspark 1, B-3590 Diepenbeek, Belgium*

^c*Fraunhofer USA, Inc., Center Midwest, 1449 Engineering Research Ct, East Lansing, MI, 48824, USA*

^d*Dept. Chemical Engineering and Materials Science, Michigan State University, East Lansing, MI, 48823, USA*

^e*Electron Microscopy for Material Science (EMAT), University of Antwerp, Groenenborgerlaan 171, 2020 Antwerp, Belgium*

^f*NANOLab Centre of Excellence, University of Antwerp, Groenenborgerlaan 171, 2020 Antwerp, Belgium*

^g*Groupe d'Etude de la Matière Condensée (GEMaC-UMR8635), CNRS, Université de Versailles St-Quentin-En-Yvelines (UVSQ), Université Paris-Saclay, 45 av des Etats Unis, 78035 Versailles Cedex, France*

Abstract

This study reports the impact of film microstructure and composition on the Young's modulus and residual stress in nanocrystalline diamond (NCD) thin films (≈ 250 nm thick) grown on silicon substrates using a linear antenna microwave plasma-enhanced chemical vapor deposition (CVD) system. Combining laser acoustic wave spectroscopy to determine the elastic properties with simple wafer curvature measurements, a straightforward method to determine the in-

Email addresses: rani.maryjoy@uhasselt.be (Rani Mary Joy), paulius.pobedinskas@uhasselt.be (Paulius Pobedinskas), ken.haenen@uhasselt.be (Ken Haenen)

¹Rani Mary Joy and Paulius Pobedinskas contributed equally to this work.

²Currently at CSIR-Institute of Minerals and Materials Technology, Bhubaneswar 751013, India

³Currently at Dept. Applied Physics, Universidad de Cádiz, 11510 Puerto Real (Cádiz), Spain

trinsic stress in NCD films is presented. Two deposition parameters are varied: 1) the substrate temperature from 400°C to 900°C, and 2) the [P]/[C] ratio from 0 ppm to 8090 ppm in the H₂/CH₄/CO₂/PH₃ diamond CVD plasma. The introduction of PH₃ induces a transition in the morphology of the diamond film, shifting from NCD with larger grains to ultra-NCD with a smaller grain size, concurrently resulting in a decrease in Young's modulus. Results show that the highest Young's modulus of (1130 ± 50) GPa for the undoped NCD deposited at 800°C is comparable to single crystal diamond, indicating that NCD with excellent mechanical properties is achievable with our process for thin diamond films. Based on the film stress results, we propose the origins of tensile intrinsic stress in the diamond films. In NCD, the tensile intrinsic stress is attributed to larger grain size, while in ultra-NCD films the tensile intrinsic stress is due to grain boundaries and impurities.

Keywords: Linear antenna CVD reactor; Nanocrystalline diamond; Young's modulus; Residual stress; Phosphorus doping.

1. Introduction

Owing to its superior mechanical and tribological properties, single crystal diamond is an attractive candidate used in various applications, however, high fabrication costs and limited up-scaling hinder its wide industrial usage [1, 2]. Polycrystalline diamond, particularly nanocrystalline diamond (NCD) and ultra-NCD (UNCD), with the prospect of large area deposition on non-diamond substrates, is an alternative to single crystal diamond for many applications such as electrochemistry, sensing and microelectromechanical systems [3–5]. It is also very attractive for protective coatings, while high thermal conductivity makes NCD a strong candidate as heat spreaders on GaN devices thereby mitigating their reliability issues [6, 7]. Despite these features, NCD is still limited in commercial usage due to its high process temperature leading to substrate damage and film adhesion issues. Of equal importance is the limited scalability in the conventional resonant cavity chemical vapor deposition (CVD) systems. Hot-

15 filament CVD technique can be used for large area NCD, but it is restricted due
16 to filament impurity incorporation and high growth temperature. By address-
17 ing these limitations, the surface wave microwave plasma-enhanced CVD (MW
18 PE CVD) systems, operated with linear, distributed or slotted antennas, are
19 promising alternatives and are capable to produce diamond coatings over large
20 area and at lower temperature [8–10].

21 Concerning the diamond coatings, an essential property for thin film based
22 applications is the tunability of residual stress generated in the coatings. The
23 main origins of residual stress in films are the thermal stress and intrinsic stress.
24 Thus, the choice of substrate and deposition conditions determine the residual
25 stress in thin films [11, 12]. A wide range of values for the mechanical prop-
26 erties of diamond films and models for residual stress generation have been
27 proposed [13–16]. Although large area NCD and UNCD can be achieved in
28 the linear antenna (LA) MW PE CVD systems, very few studies focus on the
29 mechanical properties of the films grown in such deposition systems [17, 18].
30 Moreover, the determination of the Young’s modulus of thin films is challeng-
31 ing as it involves the conversion of continuous NCD films into cantilevers or
32 membranes for bulge tests and/or uses destructive techniques such as nanoin-
33 dentation that are influenced by the film surface roughness and the underlying
34 substrate [13, 19]. In this study, we use an alternative non-destructive laser-
35 induced surface acoustic wave technique for the Young’s modulus analysis of
36 diamond films. This technique does not require any sample preparation such
37 as smoothing or cross-sectioning and is mostly conducted on the substrate/thin
38 film systems used for the actual application. Compared to nanoindentation and
39 as long as the materials allow the propagation of a sound wave, it can be applied
40 to many thin film and surface layers, ranging from ultra-thin (< 5 nm) to thick
41 (several μm) from very hard to porous materials [20, 21].

42 It is well known that doping enhances the electronic properties of diamond,
43 the most common dopants being boron and phosphorus, which make diamond a
44 p- and n-type semiconductor, respectively. Most of previous studies report the
45 diamond doping process using resonant cavity systems, while studies carried out

46 by Taylor *et al.* report on boron-doped NCD layers in the LA MW PE CVD
47 system [18, 22, 23]. Considering that diamond deposition in Ar or N₂ based
48 plasma generates UNCD, it is also worth exploring how phosphine (PH₃) addi-
49 tion in the H₂/CH₄/CO₂ plasma influences film properties. However, no studies
50 on phosphorus incorporation into NCD nor PH₃ addition as an impurity in the
51 linear antenna system have been reported. Janssen *et al.* have demonstrated
52 phosphorus incorporation in NCD under high substrate temperature conditions
53 in resonant cavity system [24]. Hence, it is of interest to extend the study to
54 high-temperature process conditions and investigate the possibility of n-type
55 doping in LA MW PE CVD diamond films.

56 In this work, we report the first results on Young’s modulus, film stress and
57 phosphorus incorporation in LA MW PE CVD diamond films. We systemati-
58 cally investigate the morphological changes, film composition and correlate these
59 properties with the residual stress in the (U)NCD thin films grown at various
60 substrate temperatures and PH₃ concentrations in the CVD growth plasma. A
61 control group of undoped diamond process at different substrate temperatures
62 is also included, allowing us to decouple the influence of substrate temperature
63 from PH₃ addition to the CVD plasma. By using a combination of two charac-
64 terization techniques, laser surface acoustic wave and wafer curvature method,
65 the Young’s modulus and residual stress are measured in a simple and straight-
66 forward manner, allowing us to determine the origins of intrinsic stress, i.e. the
67 process parameters to control the film stress are easily identified.

68 2. Experimental

69 Polished single crystal (100)-oriented 200 μm silicon substrates with an aver-
70 age roughness < 0.5 nm were used for the experiments. Substrates with 1×1 cm²
71 dimensions were used for all characterization techniques except for the laser-
72 induced surface acoustic wave technique for which 2-inch silicon wafers were
73 necessary. The substrates were dry-cleaned using an oxygen (O₂) gas discharge
74 plasma [25].

Table 1: Overview of process variables in this study.

Experiment series	T ($^{\circ}\text{C}$)	$[\text{P}]/[\text{C}]$ (ppm)
PH ₃ -series	400	0 to 8090
PH ₃ -T-series	400 to 900	8090
Undoped-T-series	400 to 900	0

75 After the treatment the substrates were seeded with nanodiamond (ND)
 76 particles by drop-casting a water-based ND colloid onto the substrate surface
 77 and covering it completely, followed by deionized water rinsing and spin drying
 78 steps. The ND colloid was prepared from detonation ND slurry provided by the
 79 NanoCarbon Institute Co., Ltd, Japan. The size of the NDs is 5 to 7 nm and
 80 the zeta-potential of the colloid is (49 ± 5) mV.

81 The diamond films were deposited either using a gas mixture of H₂/CH₄/CO₂
 82 (undoped), or with PH₃ addition to the gas mixture. The addition of CO₂ to
 83 the gas mixture was used to enhance the etching of sp² carbon phase. The
 84 PH₃ gas precursor with a concentration of 1000 ppm in H₂ was used for the
 85 experiments. Three series of diamond growth experiments on the ND seeded
 86 substrates were done in the LA MW PE CVD reactor (Tab. 1). For each sample
 87 series, one deposition parameter was varied, i.e. $[\text{P}]/[\text{C}]$ from 0 ppm (undoped)
 88 up to 8090 ppm at 400 $^{\circ}\text{C}$ for the PH₃-series, and substrate temperature (T) from
 89 400 $^{\circ}\text{C}$ to 900 $^{\circ}\text{C}$ at $[\text{P}]/[\text{C}]$ ratio of 8090 ppm (PH₃-T-series) or 0 ppm (undoped-
 90 T-series) gas compositions. The sample stage was heated by a resistive heater
 91 and T was measured by a thermocouple inside the stage. Before plasma ignition,
 92 the substrates were maintained at the set temperature. For all depositions the
 93 following parameters were kept constant: 5600 W of MW power in continuous
 94 wave mode, a working pressure of 22 Pa, a total gas flow of 150 sccm, a gas com-
 95 position of 5% CH₄ and 6% CO₂ in H₂, and sample-to-antenna distance of 5 cm.
 96 The film thickness was monitored by in-situ laser reflection interferometry with
 97 a laser wavelength of 405 nm. Depending on the chosen process conditions, the
 98 film growth rate varied between 50 nm/h and 130 nm/h, hence the deposition

99 time was adapted so that a total (U)NCD thin film thickness of about 250 nm
100 was obtained for each sample.

101 The samples chosen for transmission electron microscopy (TEM) were pre-
102 pared using a FEI Helios 650 dual-beam Focused Ion Beam (FIB) device as a
103 FIB lamella. Four-dimensional scanning TEM (4D STEM) was performed on a
104 X-Ant-EM instrument operated at 300 keV. The 4D STEM experiment was per-
105 formed by raster scanning an electron probe, with a convergence angle 1 mrad,
106 and acquiring a diffraction pattern at every probe position with a resolution of
107 ≈ 2 nm.

108 The samples were characterized by confocal micro-Raman measurements
109 using an argon ion laser ($\lambda_{\text{exc.}} = 488$ nm) with a Horiba Jobin Yvon T64000
110 spectrometer. Secondary ion mass spectrometry (SIMS) measurements (raster
111 area of $150 \times 150 \mu\text{m}^2$) were carried out on the sample deposited at a [P]/[C]
112 ratio of 8090 ppm and substrate temperature of 900°C to detect the impurities
113 present in the film. Positive primary ions with a Cs^+ source are set to 10 keV
114 and an incidence angle of 23° with respect to the surface normal of the sample.
115 The secondary ions are detected in the negative mode (sample bias at -5 kV).

116 X-ray reflectivity (XRR) was carried out for film density analysis with an X-
117 ray diffraction (XRD, Rigaku SmartLab) system with monochromatized $\text{Cu K}\alpha_1$
118 incident X-ray beam (1.541 \AA). The measurement ranged from 0° to 2° with a
119 step size of 0.0004° at $0.48^\circ/\text{min}$, whereas the analysis of the diffractograms was
120 performed between 0.4° to 0.6° with the GlobalFit software (Rigaku Ver.2.1.1).
121 The material model for the fitting by the least mean square method consisted of
122 a silicon substrate with an infinite thickness, a density of 2.33 g/cm^3 , roughness
123 of 0.3 nm and an (U)NCD film thickness of 250 nm. The NCD density and rough-
124 ness were subject to refinement, constraining the density between 2.00 g/cm^3
125 and 3.52 g/cm^3 . The apparent Young's modulus of the NCD films was deter-
126 mined by the laser surface acoustic wave technique (LAwave[®], Fraunhofer USA
127 Center Midwest CMW) [26, 27]. In this method, laser pulses ($\lambda = 337$ nm,
128 maximum power of 12 mW, pulse duration of 3 ns) absorbed by the substrate
129 generate surface acoustic waves. The low power density of the laser pulse is

130 sufficiently small for any change of state in the diamond film [28]. The waves
131 propagate along the surface with amplitude decaying exponentially within the
132 material. Due to this behavior, the surface acoustic wave is very sensitive
133 to surface layers and modifications with elastic properties and density devi-
134 ating from the bulk material. The penetration depth of the surface acoustic
135 wave depends on frequency. The higher the frequency the lower the penetration
136 depth. This method can be applied for thin films that are thinner than 50 nm.
137 The wave signal was recorded with a 500 MHz digital oscilloscope averaged over
138 64 pulses in a frequency range from 40 MHz to 200 MHz and a scan length of
139 20 mm. The dispersion of the surface acoustic waves is a function of the sub-
140 strate and film thickness, Poisson’s ratio, film density and the Young’s modulus.
141 The applied material model consists of the substrate and film properties. The
142 substrate properties were determined from an uncoated reference wafer. Due to
143 linear dispersion for the investigated diamond films, fitting of only one unknown
144 – the Young’s modulus of the diamond film could be achieved. Hence, for all
145 LAwave[®] measurements in this study, the Poisson’s ratio of the films was set to
146 0.12 (Fig. S1) [29]. The film density values for each sample were derived from
147 XRR measurements. Using the method of non-linear least squares curve fitting
148 the Young’s modulus of the diamond thin films was determined.

149 The in-plane residual stress component in the films was calculated by the
150 Stoney equation [30–32]. The substrate curvatures before and after diamond
151 CVD were obtained from line scans measurements with a Bruker DekTakXT[®]
152 stylus profilometer. The elastic constants of the Si substrate were taken from
153 the literature [33].

154 **3. Results**

155 *3.1. Film morphology and composition*

156 Figure 1 shows the 4D-STEM correlation coefficient maps and the corre-
157 sponding cross-sectional SEM images of four samples in this study. The samples
158 are diamond thin films deposited at substrate temperature of 400°C or 900°C

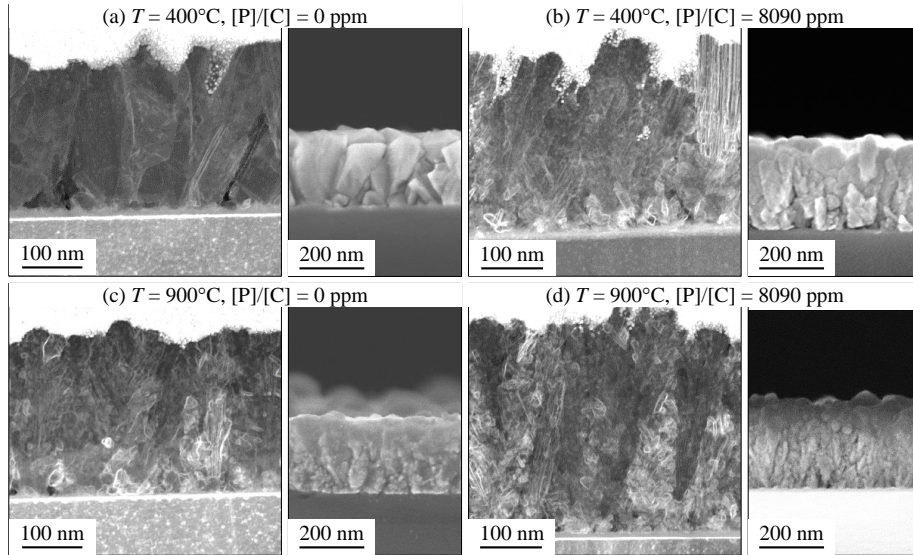


Figure 1: (a-d) 4D-STEM correlation coefficient maps (left) and cross-sectional SEM (right) images of the diamond films deposited with $[P]/[C]$ ratio of 0 ppm and 8090 ppm at 400°C and 900°C, respectively. The white lines indicate the presence of grain boundaries.

159 and with the lowest $[P]/[C]$ ratio of 0 ppm (undoped) or the highest $[P]/[C]$ ratio
 160 of 8090 ppm. The correlation coefficient maps are constructed from the differ-
 161 ences between neighboring diffraction patterns, with the white regions in the
 162 STEM images indicating grain boundaries. Of the four samples, the undoped
 163 400°C sample (Fig. 1(a)) has the largest grains with least grain boundaries. In
 164 contrast, the $[P]/[C] = 8090$ ppm sample deposited at 400°C (Fig. 1(b)) shows a
 165 complex microstructure with significantly smaller grains and more grain bound-
 166 aries. Thus, it can be confirmed that addition of PH_3 at a $[P]/[C]$ ratio of
 167 8090 ppm to the diamond CVD plasma leads to grain size reduction. A gradual
 168 film morphology transition, from faceted to dendrite-like features with smaller
 169 grains, with increasing $[P]/[C]$ ratio (PH_3 -series at 400°C) can be seen in Fig-
 170 ure S2(a). A reduced grain size is also observed for the undoped sample de-
 171 posited at 900°C (Fig. 1(c)). In this case, the grain size reduction is observed
 172 only at the highest substrate temperature of 900°C (Figs S2(c) and S3). The
 173 NCD film grown with the highest $[P]/[C]$ ratio at 900°C (Fig. 1(d)) also has a

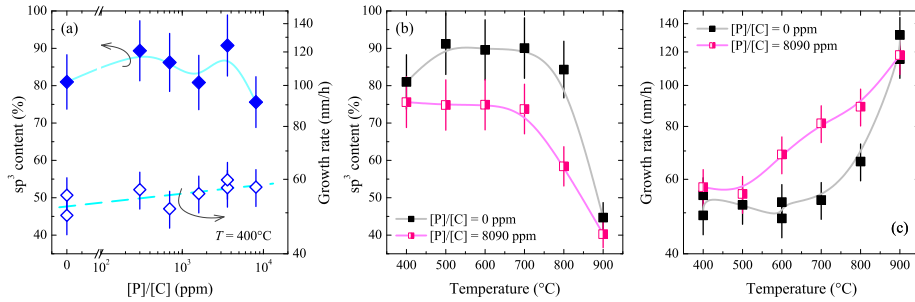


Figure 2: (a) sp^3 content in PH_3 -series samples grown at $T = 400^\circ C$ and their respective growth rates. The sp^3 content (b) in PH_3 -T-series and undoped-T-series samples, and their corresponding growth rates (c).

174 complex morphology. While clusters of smaller diamond grains are observed,
 175 there are no notable distinctions compared to the film deposited at $400^\circ C$ with
 176 the highest $[P]/[C]$ ratio.

177 In addition to the morphology changes, the diamond content of the films also
 178 changes with the growth conditions. Figure 2 shows the diamond content in the
 179 films qualitatively estimated from the Raman spectra of the samples (Fig. S4).
 180 The sp^3 content remains almost constant at $80 \pm 10\%$ for the PH_3 -series sam-
 181 ples (Fig. 2(a)). As expected from the faceted morphology, the undoped di-
 182 amond films showed the highest amount of sp^3 bonded carbon ($\approx 90\%$) with
 183 the maximum from $500^\circ C$ to $700^\circ C$ (Fig. 2(b)). Both the temperature series
 184 samples show similar trends – an increase in temperature above $800^\circ C$ leads to
 185 a significant reduction in the amount of sp^3 bonded carbon ($\approx 40\%$) for both
 186 $[P]/[C] = 8090$ ppm and the undoped layers and increasing growth rate content
 187 in the diamond films (Fig. 2(c)).

188 Thus far, phosphorus is reported to successfully incorporate in diamond
 189 layers only at elevated temperature ($> 800^\circ C$) [24, 34]. Hence, the sample de-
 190 posited at $[P]/[C] = 8090$ ppm and at a substrate temperature of $900^\circ C$ was
 191 chosen for SIMS analysis (Fig. 3). The depth profiling results show phospho-
 192 rus incorporation with uniform concentration throughout the thickness of the
 193 diamond layer. Although this result confirms that phosphorus is present in the

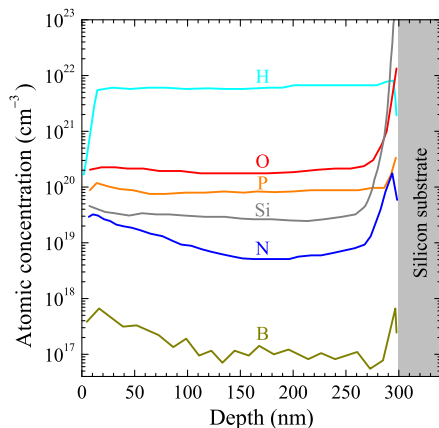


Figure 3: SIMS depth profile of the diamond film deposited with $[P]/[C]$ ratio of 8090 ppm at 900°C .

194 bulk and in high concentration ($4.2 \times 10^{19} \text{ cm}^{-3}$), it should be kept in mind that
 195 impurities are known to incorporate in grain boundaries and in non-diamond
 196 phases [35–37]. Hence, it may not be representative of the actual phosphorus
 197 concentration within the diamond grain. Additional impurities detected in the
 198 film are H, O, Si, N and B. All impurities except boron are present in high
 199 levels ($> 5 \times 10^{18} \text{ cm}^{-3}$). The presence of silicon and oxygen is attributed to the
 200 quartz tube etching during the CVD process [8], while residual N present in the
 201 deposition chamber is due to the base pressure ($1 \times 10^{-4} \text{ mbar}$) of the deposition
 202 system. The boron concentration, between $6 \times 10^{16} \text{ cm}^{-3}$ and $6 \times 10^{17} \text{ cm}^{-3}$, is
 203 unexpected as there is no boron dopant source in the process. Hence, its ori-
 204 gin is unclear. In addition to SIMS, measurements carried out with EDX and
 205 XPS techniques also confirm the variations in film composition among samples
 206 grown with different deposition conditions (Figs S5 and S6). Thus, from the
 207 above results it can be inferred that the film microstructure as well as the film
 208 composition change with the CVD diamond growth conditions.

209 3.2. Young’s modulus and in-plane residual stress

210 The Young’s modulus (E) of the diamond films also varies with the depo-
 211 sition conditions (Fig. 4). The values of E are between $(450 \pm 50) \text{ GPa}$ and

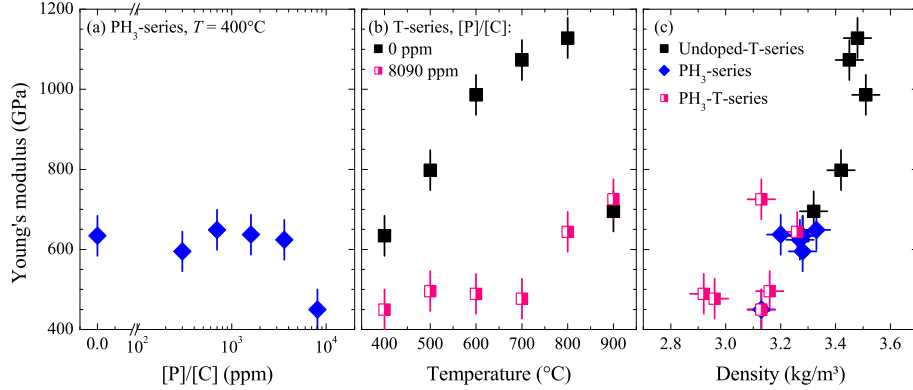


Figure 4: Young's modulus of the diamond thin films: (a) PH₃-series, (b) PH₃-T-series and undoped-T-series, and (c) Young's modulus as a function of film density.

212 (1130 ± 50) GPa, with the highest for the undoped NCD layers. The PH₃-
 213 series samples have almost constant E values of ≈ 630 GPa except for the high-
 214 est [P]/[C] ratio where a drop to ≈ 450 GPa is observed (Fig. 4(a)). For the
 215 undoped-T-series films, E steadily increases until 800°C and sharply reduces
 216 at the highest substrate temperature of 900°C (Fig. 4(b)). On the other hand,
 217 the increasing substrate temperature has a negligible effect on E for the PH₃-
 218 T-series up to 700°C beyond which an increase is observed. It should be noted
 219 that the highest values of E for the undoped diamond sample is comparable
 220 to that of single crystal diamond and achieved in our process with thin NCD
 221 films. Figure 4(d) shows the Young's modulus as a function of the diamond
 222 film density as determined with the XRR technique. The average film density
 223 of (3.46 ± 0.06) g/cm³ for the undoped-T-series samples is comparable to that
 224 of single crystal diamond (3.52 g/cm³). The PH₃-series films have a density
 225 of (3.27 ± 0.07) g/cm³ while no clear trend is observed for the PH₃-T-series
 226 samples.

227 Figure 5 shows the in-plane residual, thermal and intrinsic stress for the
 228 deposited films. The in-plane residual stress in the diamond films is evaluated
 229 from the wafer curvature measurements. All samples have compressive residual
 230 stress with the lowest value of -0.25 GPa for the film grown at [P]/[C] ratio of

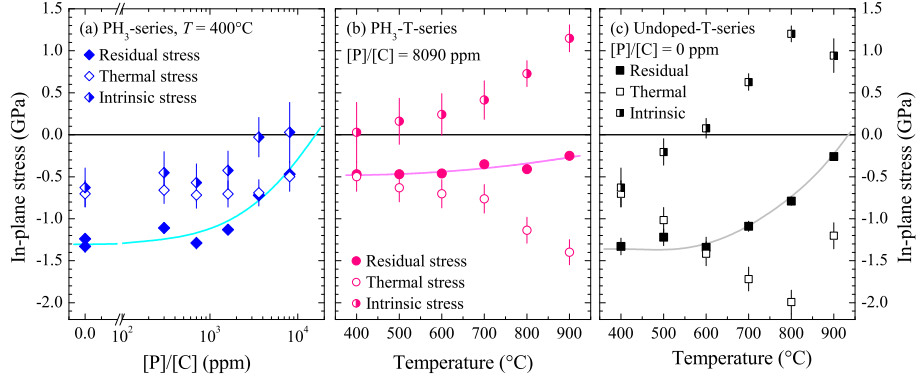


Figure 5: In-plane residual, thermal and intrinsic stress of the (U)NCD films: (a) PH₃-series, (b) PH₃-T-series, and (c) undoped-T-series.

231 8090 ppm and at a substrate temperature of 900°C. In general, the origins of the
 232 residual stress in thin films are due to: (i) the mismatch between the lattices of
 233 the substrate and the film, (ii) due to a thermal expansion coefficient difference,
 234 which generates the thermal stress when cooling down to room temperature after
 235 deposition, and (iii) the intrinsic stress, which depends on the CVD deposition
 236 conditions [11]. As the diamond growth occurs on ND seeds and not directly on
 237 the silicon substrate, the lattice mismatch is not considered in this study. The
 238 thermal stress (σ) is expressed as:

$$\sigma = \frac{E}{1 - \nu} (\alpha_{\text{film}} - \alpha_{\text{sub.}}) (T - T_0) \quad (1)$$

239 with E and ν the Young's modulus and the Poisson's ratio of NCD, respec-
 240 tively, α_{film} and $\alpha_{\text{sub.}}$ the thermal expansion coefficients of thin film and sub-
 241 strate, respectively, T and T_0 the substrate temperature at film deposition and
 242 room temperature, respectively. The thermal expansion coefficient values are
 243 reported in literature [38], and Young's modulus values were experimentally
 244 determined. The Young's modulus values stayed almost constant with Pois-
 245 son's ratio (Fig. S1), hence a Poisson's ratio of 0.12 was chosen for Young's
 246 modulus determination as well as for thermal stress calculations [29, 39]. Once
 247 the thermal stress for each deposition is calculated, it can be subtracted from
 248 the residual stress giving the value of the intrinsic stress, which can then be

249 correlated with the film properties.

250 For the PH₃-series, the deposition temperature is constant (400°C) and E
251 values remain almost constant (≈ 630 GPa), except for the sample deposited at
252 the highest [P]/[C] ratio. Therefore, the calculated thermal stress is compressive
253 and vary between -0.34 GPa and -0.36 GPa for all PH₃-series samples except
254 at the highest [P]/[C] ratio for which it is -0.25 GPa. With the increase in
255 substrate temperature, the thermal stress increases systematically for both of
256 the T-series, except for the undoped film at 900°C. Again, this deviation is due
257 to the drop in the value of Young’s modulus. The evaluated intrinsic stress
258 is compressive for the PH₃-series and decreases with increasing [P]/[C] ratio.
259 While, a transition from compressive to tensile intrinsic stress is observed at
260 400°C and 600°C for the PH₃-T-series and undoped-T-series, respectively.

261 4. Discussion

262 4.1. Film morphology and film composition

263 Depending on the CVD process conditions, the samples have different mi-
264 crostructure, ranging from randomly faceted NCD to a cauliflower-like film with
265 finer grains of ultra-NCD. The UNCD process reported earlier in N₂-based, Ar-
266 based, or CH₄-rich plasmas is primarily attributed to impurity-related surface
267 processes due to changes in plasma chemistry and surface kinetics resulting in
268 smaller grains [40–42]. In our samples, the morphology transition for the PH₃-
269 series samples confirms that phosphine-based CVD diamond growth plasma with
270 [P]/[C] ratio of 8090 ppm in the linear antenna CVD system is an impurity driven
271 process. As comparable morphology changes is observed for the undoped layers
272 at 900°C, we propose that additional impurities, such as residual gases in the
273 chamber, may be introduced into the H₂/CH₄/CO₂ diamond growth plasma at
274 higher stage temperature. Therefore, the complex morphology featuring clus-
275 ters of smaller diamond grains (Fig. 1(d)) is suggested to originate from the
276 introduction of phosphine and other impurities into the CVD growth plasma at
277 900°C. Moreover, impurities such as silicon are also known to originate from the

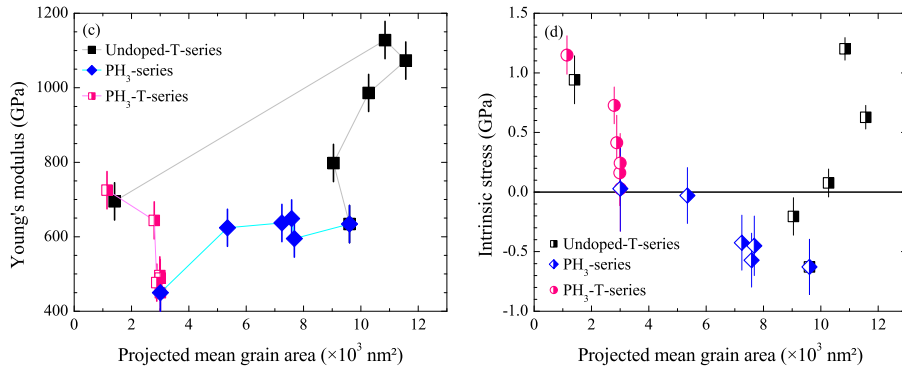


Figure 6: (a) Young's modulus and (b) intrinsic stress as a function of the projected grain area for the diamond thin films.

278 quartz tubes of the CVD system [8], leading to plate-like morphology (Fig. S2).
 279 Whether these impurities play a role in UNCD formation at higher deposition
 280 temperature (900°C), leading to transition in the film morphology, remains under
 281 investigation.

282 Earlier studies in the literature report increased sp^3 content in diamond films
 283 fabricated at higher substrate temperature in the resonant cavity MW PE CVD
 284 reactor [43, 44] and LA MW PE CVD reactor [45]. Our results are contrary
 285 – the samples have lower sp^3 bonded carbon content at the highest substrate
 286 temperature and can be explained by the impurity driven transition to UNCD
 287 process [46, 47].

288 4.2. Young's modulus and in-plane residual stress

289 The Young's modulus values obtained for the diamond films can be eluci-
 290 dated by considering the projected grain areas (deduced from the SEM images,
 291 Fig. S2). All values, except for the increased E at 800°C and 900°C for the PH₃-
 292 T-series, correlate well with the corresponding projected diamond grain areas,
 293 with higher E for larger grain areas (Fig. 6(a)). Thus, it can be confirmed that
 294 the Young's modulus of the diamond films depends on the CVD process condi-
 295 tions. Prior reports on NCD process, associate lower Young's modulus with
 296 smaller grains (i.e. more grain boundaries) [13, 14, 19, 48]. A theoretical study

297 by Sha *et al.* shows a direct correlation between the decrease in Young’s mod-
298 ulus and the increase in the density of grain boundaries in UNCD [49], while
299 Fallon *et al.*, using TEM, observed amorphous carbon at the grain boundaries
300 and at the edges of the CVD diamond grains [50]. We can hence expect that
301 diamond films with smaller grains, thus with a higher fraction of grain bound-
302 aries and amorphous carbon, result in a lower Young’s modulus than samples
303 with larger grains and less grain boundaries.

304 The intrinsic stress of diamond films is dependent on the CVD conditions
305 – the film morphology, impurities and grain boundaries are known to impact
306 the intrinsic stress of the grown film [51]. It is generally accepted that the
307 compressive intrinsic stress is attributed to non-diamond phases, hydrogen con-
308 tent and/or impurities in the layer[52]. Tensile intrinsic stress in diamond films
309 are reported to be generated by dislocations, voids and grain boundaries ex-
310 plained using the grain boundary model[16, 52, 53]. The PH₃-series samples
311 exhibit compressive intrinsic stress, with a non-diamond content of less than
312 20%. However, the samples with even higher non-diamond content, such as
313 those deposited at 900°C, display tensile intrinsic stress. These observations
314 are contrary to the expected results, hence the non-diamond content alone can-
315 not explain the origins of intrinsic stress.

316 In our samples, we explain the origins of intrinsic stress on the basis of
317 film microstructure. Our results (Fig. 6(b)) show undoped-T-series samples
318 with largest grain areas have tensile intrinsic stress. High quality diamond
319 with tensile stress are reported to arise from the onset of grain growth[12]. On
320 the contrary, it can be seen that as the area of grains reduces (density of grain
321 boundaries rises), the tensile intrinsic stress dominates, and the samples with the
322 smallest grain area demonstrate the highest tensile stress. Thus, the presence of
323 grain boundaries generating tensile stress can be supported. The incorporation
324 of trans-polyacetylene (TPA) in UNCD films with smaller grains also generates
325 tensile intrinsic stress [54]. The PH₃-T-series samples have prominent TPA peak
326 in the Raman spectra (Fig. S4) and also contribute to the intrinsic tensile stress
327 formation. The film density variation between $(2.92 \pm 0.05) \text{ g/cm}^3$ and $(3.13 \pm$

328 0.05) g/cm³ for the PH₃-T-series samples indicate film composition differences,
329 i.e. changes in the carbon matrix surrounding the grains occur. We can hence
330 conclude that tensile intrinsic stress is generated in high quality films with larger
331 grains, while in UNCD the presence of grains boundaries, the incorporation
332 of TPA and impurities in matrix surrounding the grains contribute to tensile
333 intrinsic stress generation in the samples.

334 5. Conclusion

335 In this study, we systematically investigated the Young's modulus and resid-
336 ual stress of diamond films deposited with the linear antenna CVD system. The
337 main conclusions are summarized as follows:

- 338 1. The linear antenna CVD system can be used for the growth of NCD with
339 enhanced mechanical properties. The 250 nm thick undoped NCD films
340 grown at 800°C demonstrated the Young's modulus of (1130 ± 50) GPa
341 and film density of (3.46 ± 0.05) g/cm³, which are comparable to single
342 crystal diamond.
- 343 2. The addition of PH₃ to the H₂/CH₄/CO₂ diamond CVD plasma leads to
344 diamond films with reduced grain size, which is the cause of the Young's
345 modulus reduction due to amorphous carbon within the grain boundaries.
- 346 3. Tensile intrinsic stress in diamond films is microstructure-dependent and
347 generated with higher magnitudes either in films with the smallest grain
348 areas or in those with the largest grains. Additionally, the incorporation
349 of TPA contribute to the tensile stress generation.
- 350 4. The incorporation of phosphorus in NCD thin films with a concentration
351 of up to 4.2×10^{19} cm⁻³ as shown by SIMS analysis marks a significant
352 milestone for linear antenna type CVD systems. These findings pave the
353 way for advancing to the next stages in fabricating large area phosphorus-
354 doped diamond films.

355 **Acknowledgments**

356 This work was financially supported by the Methusalem NANO network, the
357 Research Foundation – Flanders (FWO) via Project G0D4920N, and the COR-
358 NET project nr 263-EN "ULTRAHARD: Ultrahard optical diamond coatings"
359 (2020–2021).

360 **References**

- 361 [1] J.-C. Arnault, S. Saada, V. Ralchenko, Chemical vapor deposition single-
362 crystal diamond: A review, *Phys. Status Solidi RRL* 16 (1) (2022) 2100354.
363 [doi:10.1002/pssr.202100354](https://doi.org/10.1002/pssr.202100354).
- 364 [2] M. Schreck, Growth of Single Crystal Diamond Wafers for Future Device
365 Applications, John Wiley & Sons, Ltd, 2021, Ch. 20, pp. 583–631. [doi:](https://doi.org/10.1002/9783527824724.ch20)
366 [10.1002/9783527824724.ch20](https://doi.org/10.1002/9783527824724.ch20).
- 367 [3] N. Yang, J. S. Foord, X. Jiang, Diamond electrochemistry at the nanoscale:
368 A review, *Carbon* 99 (2016) 90–110. [doi:10.1016/j.carbon.2015.11.](https://doi.org/10.1016/j.carbon.2015.11.061)
369 [061](https://doi.org/10.1016/j.carbon.2015.11.061).
- 370 [4] S. Drijkoningen, S. D. Janssens, P. Pobedinskas, S. Koizumi, M. K.
371 Van Bael, K. Haenen, The pressure sensitivity of wrinkled B-doped
372 nanocrystalline diamond membranes, *Sci. Rep.* 6 (1) (2016). [doi:10.1038/](https://doi.org/10.1038/srep35667)
373 [srep35667](https://doi.org/10.1038/srep35667).
- 374 [5] O. Auciello, D. M. Aslam, Review on advances in microcrystalline,
375 nanocrystalline and ultrananocrystalline diamond films-based micro/nano-
376 electromechanical systems technologies, *J. Mater. Sci.* 56 (12) (2021) 7171–
377 7230. [doi:10.1007/s10853-020-05699-9](https://doi.org/10.1007/s10853-020-05699-9).
- 378 [6] L. Vandenbulcke, M. De Barros, Deposition, structure, mechanical prop-
379 erties and tribological behavior of polycrystalline to smooth fine-grained
380 diamond coatings, *Surf. Coat. Technol.* 146-147 (2001) 417–424. [doi:](https://doi.org/10.1016/S0257-8972(01)01407-4)
381 [10.1016/S0257-8972\(01\)01407-4](https://doi.org/10.1016/S0257-8972(01)01407-4).

- 382 [7] Y. Zhou, R. Ramaneti, J. Anaya, S. Korneychuk, J. Derluyn, H. Sun,
383 J. Pomeroy, J. Verbeeck, K. Haenen, M. Kuball, Thermal characterization
384 of polycrystalline diamond thin film heat spreaders grown on GaN HEMTs,
385 *Appl. Phys. Lett.* 111 (4) (2017) 041901. doi:10.1063/1.4995407.
- 386 [8] S. Drijkoningen, P. Pobedinskas, S. Korneychuk, A. Momot, Y. Balasub-
387 ramaniam, M. K. Van Bael, S. Turner, J. Verbeeck, M. Nesládek, K. Hae-
388 nen, On the origin of diamond plates deposited at low temperature, *Cryst.*
389 *Growth Des.* 17 (8) (2017) 4306–4314. doi:10.1021/acs.cgd.7b00623.
- 390 [9] H.-A. Mehedi, J. Achard, D. Rats, O. Brinza, A. Tallaire, V. Mille,
391 F. Silva, C. Provent, A. Gicquel, Low temperature and large area de-
392 position of nanocrystalline diamond films with distributed antenna array
393 microwave-plasma reactor, *Diam. Relat. Mater.* 47 (2014) 58–65. doi:
394 10.1016/j.diamond.2014.05.004.
- 395 [10] J. Zalieckas, P. Pobedinskas, M. M. Greve, K. Eikehaug, K. Haenen,
396 B. Holst, Large area microwave plasma CVD of diamond using compos-
397 ite right/left-handed materials, *Diam. Relat. Mater.* 116 (2021) 108394.
398 doi:10.1016/j.diamond.2021.108394.
- 399 [11] C. T. Kuo, C. R. Lin, H. M. Lien, Origins of the residual stress in CVD
400 diamond films, *Thin Solid Films* 290-291 (1996) 254–259. doi:10.1016/
401 S0040-6090(96)09016-5.
- 402 [12] N. Shang, C. Lee, Z. Lin, I. Bello, S. Lee, Intrinsic stress evolution in
403 diamond films prepared in a CH₄-H₂-NH₃ hot filament chemical vapor
404 deposition system, *Diam. Relat. Mater.* 9 (7) (2000) 1388–1392. doi:
405 10.1016/S0925-9635(00)00265-X.
- 406 [13] O. Williams, A. Kriele, J. Hees, M. Wolfer, W. Müller-Sebert, C. Nebel,
407 High Young’s modulus in ultra thin nanocrystalline diamond, *Chem. Phys.*
408 *Lett.* 495 (1) (2010) 84–89. doi:10.1016/j.cplett.2010.06.054.

- 409 [14] M. Mohr, A. Caron, P. Herbeck-Engel, R. Bennewitz, P. Gluche, K. Brühne,
410 H.-J. Fecht, Young's modulus, fracture strength, and Poisson's ratio of
411 nanocrystalline diamond films, *J. Appl. Phys.* 116 (12) (2014) 124308. doi:
412 [10.1063/1.4896729](https://doi.org/10.1063/1.4896729).
- 413 [15] C. Hua, X. Yan, J. Wei, J. Guo, J. Liu, L. Chen, L. Hei, C. Li, Intrinsic
414 stress evolution during different growth stages of diamond film, *Diam.*
415 *Relat. Mater.* 73 (2017) 62–66. doi:[10.1016/j.diamond.2016.12.008](https://doi.org/10.1016/j.diamond.2016.12.008).
- 416 [16] W. L. Wang, M. C. Polo, G. Sánchez, J. Cifre, J. Esteve, Internal stress and
417 strain in heavily boron-doped diamond films grown by microwave plasma
418 and hot filament chemical vapor deposition, *J. Appl. Phys.* 80 (3) (1996)
419 1846–1850. doi:[10.1063/1.362996](https://doi.org/10.1063/1.362996).
- 420 [17] S. S. Nicley, S. Drijkoningen, P. Pobedinskas, J. Raymakers, W. Maes,
421 K. Haenen, Growth of boron-doped diamond films on gold-coated sub-
422 strates with and without gold nanoparticle formation, *Cryst. Growth Des.*
423 19 (6) (2019) 3567–3575. doi:[10.1021/acs.cgd.9b00488](https://doi.org/10.1021/acs.cgd.9b00488).
- 424 [18] A. Taylor, L. Klimša, J. Kopeček, Z. Remeš, M. Vronka, R. Čtvrtlík,
425 J. Tomáščík, V. Mortet, Synthesis and properties of diamond - silicon
426 carbide composite layers, *J. Alloys Compd.* 800 (2019) 327–333. doi:
427 [10.1016/j.jallcom.2019.06.016](https://doi.org/10.1016/j.jallcom.2019.06.016).
- 428 [19] M. Wiora, K. Brühne, A. Flöter, P. Gluche, T. Willey, S. Kucheyev, A. Van
429 Buuren, A. Hamza, J. Biener, H.-J. Fecht, Grain size dependent mechanical
430 properties of nanocrystalline diamond films grown by hot-filament CVD,
431 *Diam. Relat. Mater.* 18 (5) (2009) 927–930. doi:[10.1016/j.diamond.](https://doi.org/10.1016/j.diamond.2008.11.026)
432 [2008.11.026](https://doi.org/10.1016/j.diamond.2008.11.026).
- 433 [20] D. Schneider, P. Siemroth, T. Schülke, J. Berthold, B. Schultrich, H.-H.
434 Schneider, R. Ohr, B. Peterleit, H. Hillgers, Quality control of ultra-thin
435 and super-hard coatings by laser-acoustics, *Surf. Coat. Technol.* 153 (2)
436 (2002) 252–260. doi:[10.1016/S0257-8972\(01\)01664-4](https://doi.org/10.1016/S0257-8972(01)01664-4).

- 437 [21] G. Chow, E. Uchaker, G. Cao, J. Wang, Laser-induced surface acoustic
438 waves: An alternative method to nanoindentation for the mechanical char-
439 acterization of porous nanostructured thin film electrode media, *Mech.*
440 *Mater.* 91 (2015) 333–342. doi:10.1016/j.mechmat.2015.10.005.
- 441 [22] A. Taylor, L. Fekete, P. Hubík, A. Jäger, P. Janíček, V. Mortet, J. Mistrík,
442 J. Vacík, Large area deposition of boron doped nano-crystalline diamond
443 films at low temperatures using microwave plasma enhanced chemical
444 vapour deposition with linear antenna delivery, *Diam. Relat. Mater.* 47
445 (2014) 27–34. doi:10.1016/j.diamond.2014.05.002.
- 446 [23] A. Taylor, P. Ashcheulov, P. Hubík, L. Klimša, J. Kopeček, Z. Remeš,
447 Z. Vlčková Živcová, M. Remzová, L. Kavan, E. Scheid, J. Lorinčík,
448 V. Mortet, Precursor gas composition optimisation for large area boron
449 doped nano-crystalline diamond growth by MW-LA-PECVD, *Carbon* 128
450 (2018) 164–171. doi:10.1016/j.carbon.2017.11.063.
- 451 [24] W. Janssen, S. Turner, G. Sakr, F. Jomard, J. Barjon, G. Degutis, Y.-
452 G. Lu, J. D’Haen, A. Hardy, M. V. Bael, J. Verbeeck, G. V. Tende-
453 loo, K. Haenen, Substitutional phosphorus incorporation in nanocrystalline
454 CVD diamond thin films, *Phys. Status Solidi RRL* 8 (8) (2014) 705–709.
455 doi:10.1002/pssr.201409235.
- 456 [25] P. Pobedinskas, G. Degutis, W. Dexters, W. Janssen, S. D. Janssens,
457 B. Conings, B. Ruttens, J. D’Haen, H.-G. Boyen, A. Hardy, M. K.
458 Van Bael, K. Haenen, Surface plasma pretreatment for enhanced di-
459 amond nucleation on AlN, *Appl. Phys. Lett.* 102 (20) (2013) 201609.
460 doi:10.1063/1.4807591.
- 461 [26] D. Schneider, B. Schultrich, H.-J. Scheibe, H. Ziegele, M. Griepentrog,
462 A laser-acoustic method for testing and classifying hard surface layers,
463 *Thin Solid Films* 332 (1–2) (1998) 157–163. doi:10.1016/s0040-6090(98)
464 00988-2.

- 465 [27] D. Schneider, T. Schwarz, H.-J. Scheibe, M. Panzner, Non-destructive eval-
466 uation of diamond and diamond-like carbon films by laser induced sur-
467 face acoustic waves, *Thin Solid Films* 295 (1–2) (1997) 107–116. doi:
468 [10.1016/s0040-6090\(96\)09163-8](https://doi.org/10.1016/s0040-6090(96)09163-8).
- 469 [28] J. Aussel, A. Le Brun, J. Baboux, Generating acoustic waves by laser: the-
470 oretical and experimental study of the emission source, *Ultrasonics* 26 (5)
471 (1988) 245–255. doi:[10.1016/0041-624x\(88\)90013-3](https://doi.org/10.1016/0041-624x(88)90013-3).
- 472 [29] Z. H. Shen, P. Hess, J. P. Huang, Y. C. Lin, K. H. Chen, L. C. Chen,
473 S. T. Lin, Mechanical properties of nanocrystalline diamond films, *J. Appl.*
474 *Phys.* 99 (12) (2006) 124302. doi:[10.1063/1.2203428](https://doi.org/10.1063/1.2203428).
- 475 [30] G. Stoney, The tension of metallic films deposited by electrolysis, *Proc. R.*
476 *Soc. A* 82 (1909) 172–175. doi:[10.1098/rspa.1909.0021](https://doi.org/10.1098/rspa.1909.0021).
- 477 [31] G. C. A. M. Janssen, M. M. Abdalla, F. van Keulen, B. R. Pujada,
478 B. van Venrooy, Celebrating the 100th anniversary of the Stoney equa-
479 tion for film stress: Developments from polycrystalline steel strips to sin-
480 gle crystal silicon wafers, *Thin Solid Films* 517 (6) (2009) 1858–1867.
481 doi:[10.1016/j.tsf.2008.07.014](https://doi.org/10.1016/j.tsf.2008.07.014).
- 482 [32] P. Pobedinskas, J.-C. Bolsée, W. Dexters, B. Ruttens, V. Mortet,
483 J. D’Haen, J. V. Manca, K. Haenen, Thickness dependent residual stress
484 in sputtered AlN thin films, *Thin Solid Films* 522 (2012) 180–185. doi:
485 [10.1016/j.tsf.2012.08.015](https://doi.org/10.1016/j.tsf.2012.08.015).
- 486 [33] M. A. Hopcroft, W. D. Nix, T. W. Kenny, What is the Young’s modulus of
487 silicon?, *J. Microelectromech. Syst.* 19 (2) (2010) 229–238. doi:[10.1109/
488 JMEMS.2009.2039697](https://doi.org/10.1109/JMEMS.2009.2039697).
- 489 [34] H. Kato, M. Ogura, T. Makino, D. Takeuchi, S. Yamasaki, N-type control
490 of single-crystal diamond films by ultra-lightly phosphorus doping, *Appl.*
491 *Phys. Lett.* 109 (14) (2016) 142102. doi:[10.1063/1.4964382](https://doi.org/10.1063/1.4964382).

- 492 [35] P. W. May, W. J. Ludlow, M. Hannaway, J. A. Smith, K. N. Rosser, P. J.
493 Heard, Boron doping of microcrystalline and nanocrystalline diamond films:
494 Where is the boron going?, MRS Online Proc. Lib. 1039 (2007) 1703. doi:
495 [10.1557/proc-1039-p17-03](https://doi.org/10.1557/proc-1039-p17-03).
- 496 [36] M. Sternberg, P. Zapoll, T. Frauenheim, D. M. Gruen, L. A. Curtiss,
497 Molecular dynamics simulation of impurities in nanocrystalline diamond
498 grain boundaries, MRS Online Proc. Lib. 593 (1999) 483–487. doi:
499 [10.1557/proc-593-481](https://doi.org/10.1557/proc-593-481).
- 500 [37] Y.-G. Lu, S. Turner, J. Verbeeck, S. D. Janssens, P. Wagner, K. Haenen,
501 G. Van Tendeloo, Direct visualization of boron dopant distribution and
502 coordination in individual chemical vapor deposition nanocrystalline B-
503 doped diamond grains, Appl. Phys. Lett. 101 (4) (2012) 041907. doi:
504 [10.1063/1.4738885](https://doi.org/10.1063/1.4738885).
- 505 [38] N. Woehrl, T. Hirte, O. Posth, V. Buck, Investigation of the coefficient of
506 thermal expansion in nanocrystalline diamond films, Diam. Relat. Mater.
507 18 (2) (2009) 224–228. doi:[10.1016/j.diamond.2008.10.016](https://doi.org/10.1016/j.diamond.2008.10.016).
- 508 [39] J. Philip, P. Hess, T. Feygelson, J. E. Butler, S. Chattopadhyay, K. H.
509 Chen, L. C. Chen, Elastic, mechanical, and thermal properties of nanocryst-
510 talline diamond films, J. Appl. Phys. 93 (4) (2003) 2164–2171. doi:
511 [10.1063/1.1537465](https://doi.org/10.1063/1.1537465).
- 512 [40] C.-S. Wang, H.-C. Chen, H.-F. Cheng, I.-N. Lin, Origin of platelike gran-
513 ular structure for the ultrananocrystalline diamond films synthesized in
514 H₂-containing Ar/CH₄ plasma, J. Appl. Phys. 107 (3) (2010) 034304.
515 doi:[10.1063/1.3296187](https://doi.org/10.1063/1.3296187).
- 516 [41] K. J. Sankaran, J. Kurian, H. C. Chen, C. L. Dong, C. Y. Lee, N. H. Tai,
517 I. N. Lin, Origin of a needle-like granular structure for ultrananocrystalline
518 diamond films grown in a N₂/CH₄ plasma, J. Phys. D: Appl. Phys. 45 (36)
519 (2012) 365303. doi:[10.1088/0022-3727/45/36/365303](https://doi.org/10.1088/0022-3727/45/36/365303).

- 520 [42] J. A. Cuenca, K. J. Sankaran, P. Pobedinskas, K. Panda, I.-N. Lin,
521 A. Porch, K. Haenen, O. A. Williams, Microwave cavity perturbation of
522 nitrogen doped nano-crystalline diamond films, *Carbon* 145 (2019) 740–
523 750. [doi:10.1016/j.carbon.2018.12.025](https://doi.org/10.1016/j.carbon.2018.12.025).
- 524 [43] Y. Cong, R. W. Collins, G. F. Epps, H. Windischmann, Spectroellipsometry
525 characterization of optical quality vapor-deposited diamond thin films,
526 *Appl. Phys. Lett.* 58 (8) (1991) 819–821. [doi:10.1063/1.104499](https://doi.org/10.1063/1.104499).
- 527 [44] W. Fortunato, A. J. Chiquito, J. C. Galzerani, J. R. Moro, Crystalline quality
528 and phase purity of CVD diamond films studied by Raman spectroscopy,
529 *J. Mater. Sci.* 42 (2007) 7331–7336. [doi:10.1007/s10853-007-1575-0](https://doi.org/10.1007/s10853-007-1575-0).
- 530 [45] T. Izak, O. Babchenko, M. Varga, S. Potocky, A. Kromka, Low temperature
531 diamond growth by linear antenna plasma CVD over large area, *Phys.*
532 *Status Solidi B* 249 (12) (2012) 2600–2603. [doi:10.1002/pssb.201200103](https://doi.org/10.1002/pssb.201200103).
- 533 [46] K. J. Sankaran, C.-J. Yeh, P.-Y. Hsieh, P. Pobedinskas, S. Kunuku, K.-C.
534 Leou, N.-H. Tai, I.-N. Lin, K. Haenen, Origin of conductive nanocrystalline
535 diamond nanoneedles for optoelectronic applications, *ACS Appl. Mater.*
536 *Interfaces* 11 (28) (2019) 25388–25398. [doi:10.1021/acsami.9b05469](https://doi.org/10.1021/acsami.9b05469).
- 537 [47] X. Li, J. Perkins, R. Collazo, R. J. Nemanich, Z. Sitar, Investigation of the
538 effect of the total pressure and methane concentration on the growth rate
539 and quality of diamond thin films grown by MPCVD, *Diam. Relat. Mater.*
540 15 (11) (2006) 1784–1788. [doi:10.1016/j.diamond.2006.09.008](https://doi.org/10.1016/j.diamond.2006.09.008).
- 541 [48] G. Cicala, V. Magaletti, G. Senesi, G. Carbone, D. Altamura, C. Gian-
542 nini, R. Bartali, Superior hardness and Young’s modulus of low tempera-
543 ture nanocrystalline diamond coatings, *Mater. Chem. Phys.* 144 (3) (2014)
544 505–511. [doi:10.1016/j.matchemphys.2014.01.027](https://doi.org/10.1016/j.matchemphys.2014.01.027).
- 545 [49] Z. Sha, P. Branicio, V. Sorkin, Q. Pei, Y. Zhang, Effects of grain size and
546 temperature on mechanical and failure properties of ultrananocrystalline

- 547 diamond, *Diam. Relat. Mater.* 20 (10) (2011) 1303–1309. [doi:10.1016/j.](https://doi.org/10.1016/j.diamond.2011.08.012)
548 [diamond.2011.08.012](https://doi.org/10.1016/j.diamond.2011.08.012).
- 549 [50] P. Fallon, L. Brown, Analysis of chemical-vapour-deposited diamond
550 grain boundaries using transmission electron microscopy and parallel elec-
551 tron energy loss spectroscopy in a scanning transmission electron micro-
552 scope, *Diam. Relat. Mater.* 2 (5–7) (1993) 1004–1011. [doi:10.1016/](https://doi.org/10.1016/0925-9635(93)90265-4)
553 [0925-9635\(93\)90265-4](https://doi.org/10.1016/0925-9635(93)90265-4).
- 554 [51] X. Xiao, J. Birrell, J. E. Gerbi, O. Auciello, J. A. Carlisle, Low temperature
555 growth of ultrananocrystalline diamond, *J. Appl. Phys.* 96 (4) (2004) 2232–
556 2239. [doi:10.1063/1.1769609](https://doi.org/10.1063/1.1769609).
- 557 [52] H. Windischmann, G. F. Epps, Y. Cong, R. W. Collins, Intrinsic stress in
558 diamond films prepared by microwave plasma CVD, *J. Appl. Phys.* 69 (4)
559 (1991) 2231–2237. [doi:10.1063/1.348701](https://doi.org/10.1063/1.348701).
- 560 [53] T. Anthony, Stresses generated by impurities in diamond, *Diam. Relat.*
561 *Mater.* 4 (12) (1995) 1346. [doi:10.1016/0925-9635\(95\)00317-7](https://doi.org/10.1016/0925-9635(95)00317-7).
- 562 [54] V. Buck, N. Woehrl, Tailoring the matrix in ultra-nanocrystalline diamond
563 films, *Jpn. J. Appl. Phys.* 47 (10) (2008) 8208–8213. [doi:10.1143/jjap.](https://doi.org/10.1143/jjap.47.8208)
564 [47.8208](https://doi.org/10.1143/jjap.47.8208).

Supplementary material:

The effect of microstructure and film composition on the mechanical properties of linear antenna CVD diamond thin films

Rani Mary Joy^{a,b,1}, Paulius Pobedinskas^{a,b,1}, Nina Baule^c, Shengyuan Bai^d, Daen Jannis^{e,f}, Nicolas Gauquelin^{e,f}, Marie-Amandine Pinault-Thaury^g, François Jomard^g, Kamatchi Jothiramalingam Sankaran^{a,b,2}, Rozita Rouzbahani^{a,b}, Fernando Lloret^{a,b,3}, Derese Desta^{a,b}, Jan D'Haen^{a,b}, Johan Verbeeck^{e,f}, Michael Frank Becker^c, Ken Haenen^{a,b}

^a*Institute for Materials Research (IMO), Hasselt University, Wetenschapspark 1, B-3590 Diepenbeek, Belgium*

^b*IMOMECA, IMEC vzw, Wetenschapspark 1, B-3590 Diepenbeek, Belgium*

^c*Fraunhofer USA, Inc., Center Midwest, 1449 Engineering Research Ct, East Lansing, MI, 48824, USA*

^d*Dept. Chemical Engineering and Materials Science, Michigan State University, East Lansing, MI, 48823, USA*

^e*Electron Microscopy for Material Science (EMAT), University of Antwerp, Groenenborgerlaan 171, 2020 Antwerp, Belgium*

^f*NANOLab Centre of Excellence, University of Antwerp, Groenenborgerlaan 171, 2020 Antwerp, Belgium*

^g*Groupe d'Etude de la Matière Condensée (GEMaC-UMR8635), CNRS, Université de Versailles St-Quentin-En-Yvelines (UVSQ), Université Paris-Saclay, 45 av des Etats Unis, 78035 Versailles Cedex, France*

1. Experimental details

1.1. Substrate preparation

The substrates were loaded into the chamber and pumped down until a base pressure in the vacuum chamber was below 0.5 mPa. The pressure during the O₂ gas discharge plasma was kept at 0.5 Pa. O₂ gas flow was 50 sccm. The power supply, biasing the substrate stage, was driven in a constant power mode at 300 W for 1 min. This treatment allows quick and simple removal of hydrocarbon contamination from the substrate surface and achieving high nanodiamond (ND) seeding density[1].

1.2. Film characterisation

The sample surface morphology was characterized by a Zeiss 450 FEGSEM scanning electron microscope (SEM) with Gemini 2 optics (Zeiss, Oberkochen, Germany). The surface roughness (R_q) of the films was evaluated using atomic force microscopy (AFM) with scans performed on a Bruker Multimode 8 in tapping mode. The surface chemical composition was determined by X-ray photoelectron spectroscopy (XPS) using a Physical Electronics (PHI) 5600LS electron spectrometer equipped with a 1 mm diameter spot X-ray source providing monochromatized Al K _{α} photons (1486.6 eV). Energy dispersive X-ray (EDX) spectroscopy were performed on an X-Ant-EM instrument operated at 300 keV. The EDX maps were obtained by scanning the electron beam over the sample area to get an averaged EDX signal. The processing of the EDX data is performed using the open-source software Hyperspy [2].

Email addresses: rani.maryjoy@uhasselt.be (Rani Mary Joy), paulius.pobedinskas@uhasselt.be (Paulius Pobedinskas), ken.haenen@uhasselt.be (Ken Haenen)

¹R. Mary Joy and P. Pobedinskas contributed equally to this work.

²Currently at CSIR-Institute of Minerals and Materials Technology, Bhubaneswar 751013, India

³Currently at Dept. Applied Physics, Universidad de Cádiz, 11510 Puerto Real (Cádiz), Spain

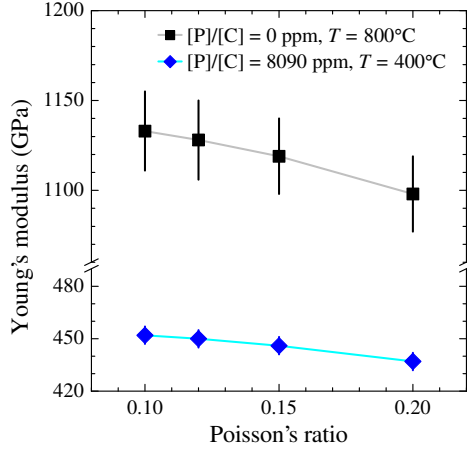


Figure S1: Young's modulus for different Poisson's ratio for the curve fitting with LAwave[®] system.

1.3. Laser-induced surface acoustic wave technique

The laser-induced surface acoustic wave technique is a versatile method for analyzing thin films by allowing surface acoustic waves to travel through the material. This approach is applicable to any material that can absorb the laser wavelength (337 nm) used. The penetration depth of surface acoustic waves depends on frequency, with higher frequencies resulting in shallower penetration due to shorter wavelengths. The technique is not limited by film thickness, as long as the equipment can detect phase velocity at the relevant frequencies. Different frequencies cater to varying film thicknesses, and even bulk materials can be analyzed with low-frequency sensors. The method is effective for thicker films, where fitting theoretical curves can extract multiple unknowns, eliminating the need for additional characterization steps like XRR analysis.

2. Results

The Raman spectra of the NCD samples contain of diamond resonance peak at 1332 cm^{-1} that corresponds to the F_{2g} resonance mode of sp^3 bonded carbon (Fig. S4). The presence of the diamond peak, although in varying peak intensities, confirm diamond formation under all deposition conditions chosen in this study. Besides the diamond signal, the spectra contain D-band ($\approx 1360\text{ cm}^{-1}$) and G-band ($\approx 1560\text{ cm}^{-1}$) resonance peaks, which correspond to disordered carbon and graphite, respectively. Also, the characteristic non-diamond phases such as trans-polyacetylene (TPA), i.e. the ν_1 -band ($\approx 1150\text{ cm}^{-1}$) and ν_3 -band ($\approx 1490\text{ cm}^{-1}$) resonance peaks, are detected, which correspond to the deformation modes of CH_x bonds [3, 4]. The sp^3 content was calculated using the following formula [5]:

$$\text{sp}^3 = \frac{75 \times I_d}{75 \times I_d + \sum I_{\text{nd}}} \quad (1)$$

where I_d is the integrated diamond peak intensity (at 1332 cm^{-1}), I_{nd} is the integrated non-diamond peak intensity. The diamond signal efficiency factor of 75 was used, because sp^2 and sp^3 bonded carbon have different sensitivity to excitation wavelength [6].

XPS was used to analyze the surface elemental composition and chemical state of phosphorus-doped NCD films grown with $[\text{P}]/[\text{C}] = 8090\text{ ppm}$ at a substrate temperature of 500°C and 900°C . Figure S5(a) shows the survey spectra that reveal minimal oxygen ($< 2\text{ at.}\%$) and fluorine ($< 6.5\text{ at.}\%$) residuals that are derived from reactor contamination. Figure S5(b) presents the C1s core-level decomposition of the films. Both films exhibit a dominant sp^3 C peak centered at around 284.4 eV and a small O-C component

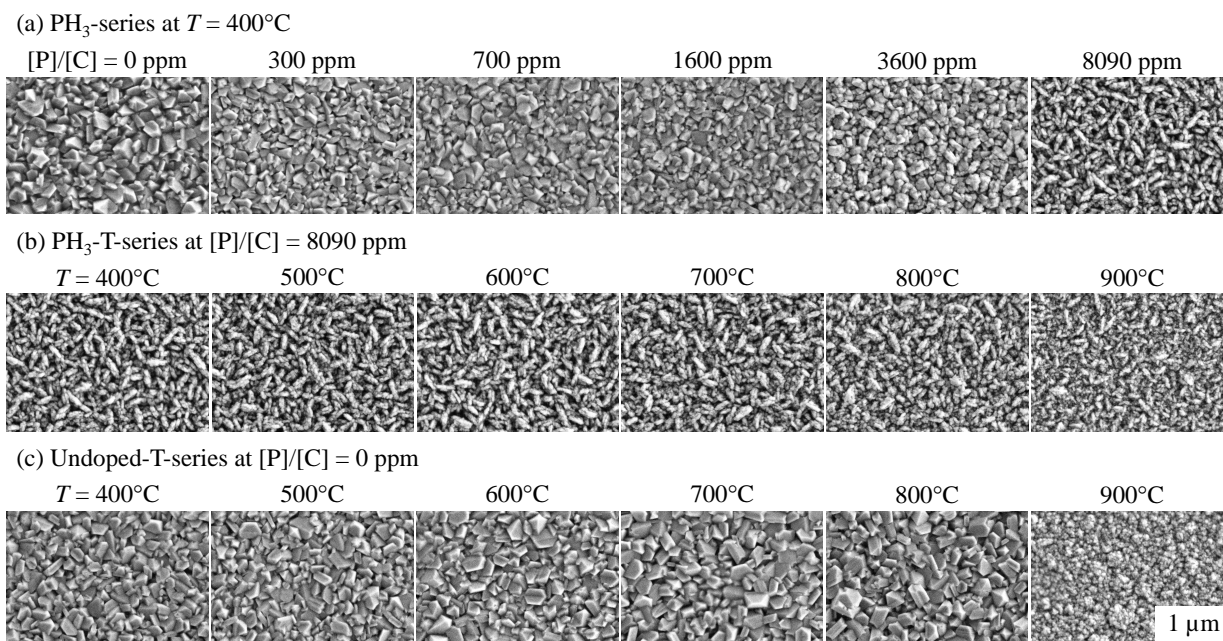


Figure S2: SEM images of the (U)NCD films: (a) PH₃-series, (b) PH₃-T-series, and (c) undoped-T-series.

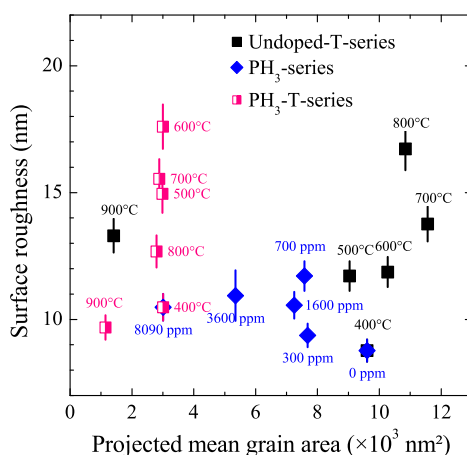


Figure S3: Surface roughness (R_q) as a function of the projected grain area of the diamond films.

(around 285.5 eV). The P2p spectra presented in Figure S5(c) show that phosphorus has been successfully incorporated into the carbon matrix for the NCD films grown at 900°C compared to those films at 500°C. The 900°C P2p spectrum is composed of core-line doublets: P2p_{1/2} peak centered around 133.1 eV and P2p_{3/2} peak centered around binding energy 132.3 eV.

Figures S6(a-d) shows the EDX mapping and spectra for the chosen samples. The silicon substrate and (U)NCD layers could be identified along with the oxygen-rich interface for all samples. However, no clear differences could be seen in the elemental content of the different diamond films. Figure S6(e) shows the EDX spectra, normalized to the carbon peak. The Cu and Ga peaks around 1 keV are associated with the sample holder of the TEM specimen and implantation from the Ga – ion beam used during focused ion beam

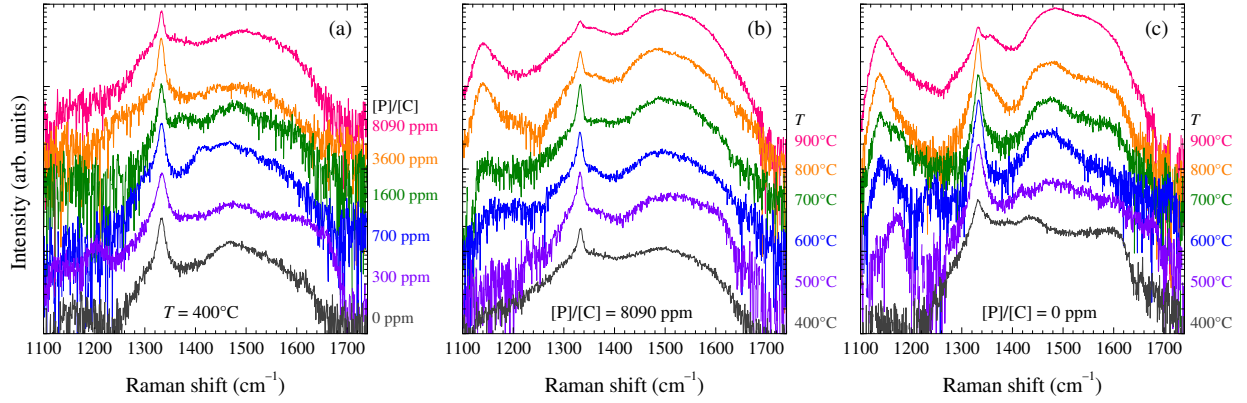


Figure S4: Raman spectra of the diamond films: (a) PH₃-series, (b) PH₃-T-series, and (c) undoped-T-series.

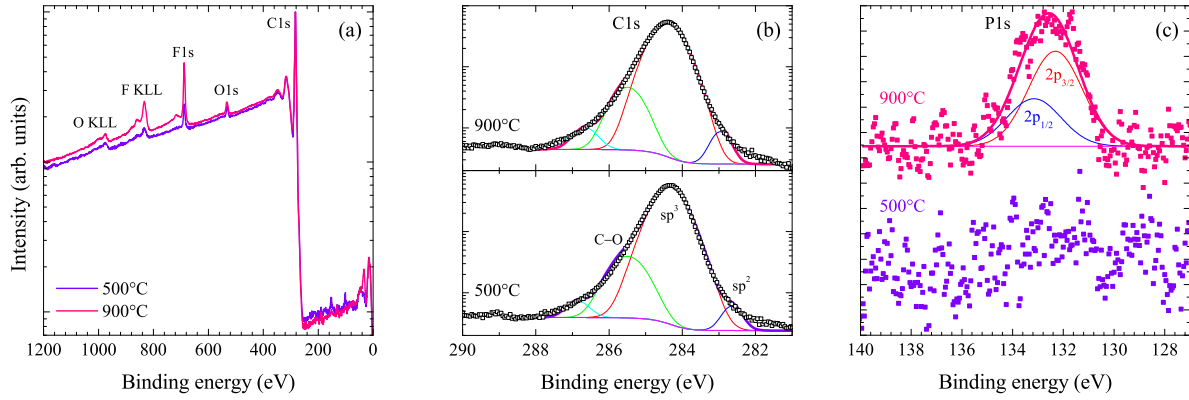


Figure S5: XPS survey (a), C1s (b) and P2p (c) spectra of phosphorus doped NCD films grown with $[P]/[C] = 8090$ ppm at a substrate temperature of 500°C and 900°C.

sample preparation, respectively. In addition to carbon, impurities such as silicon and oxygen are observed with significantly higher intensities for the films grown with PH₃ present in the plasma. The Si originates from the quartz tubes that are unavoidably slightly etched by the CVD plasma, and thus, SiO₂ could be deposited [7]. This argument is supported by the fact that the peak intensities of Si and O correlate for all the samples. The highest peak intensities for Si and O are observed for the $[P]/[C] = 8090$ ppm at 900°C sample and may be associated with their improved incorporation at higher substrate temperature. We note that phosphorus is not observed for the films deposited at $[P]/[C] = 8090$ ppm and 900°C. This is due to the P concentration below the detection limit of the characterization technique ($\approx 1\%$).

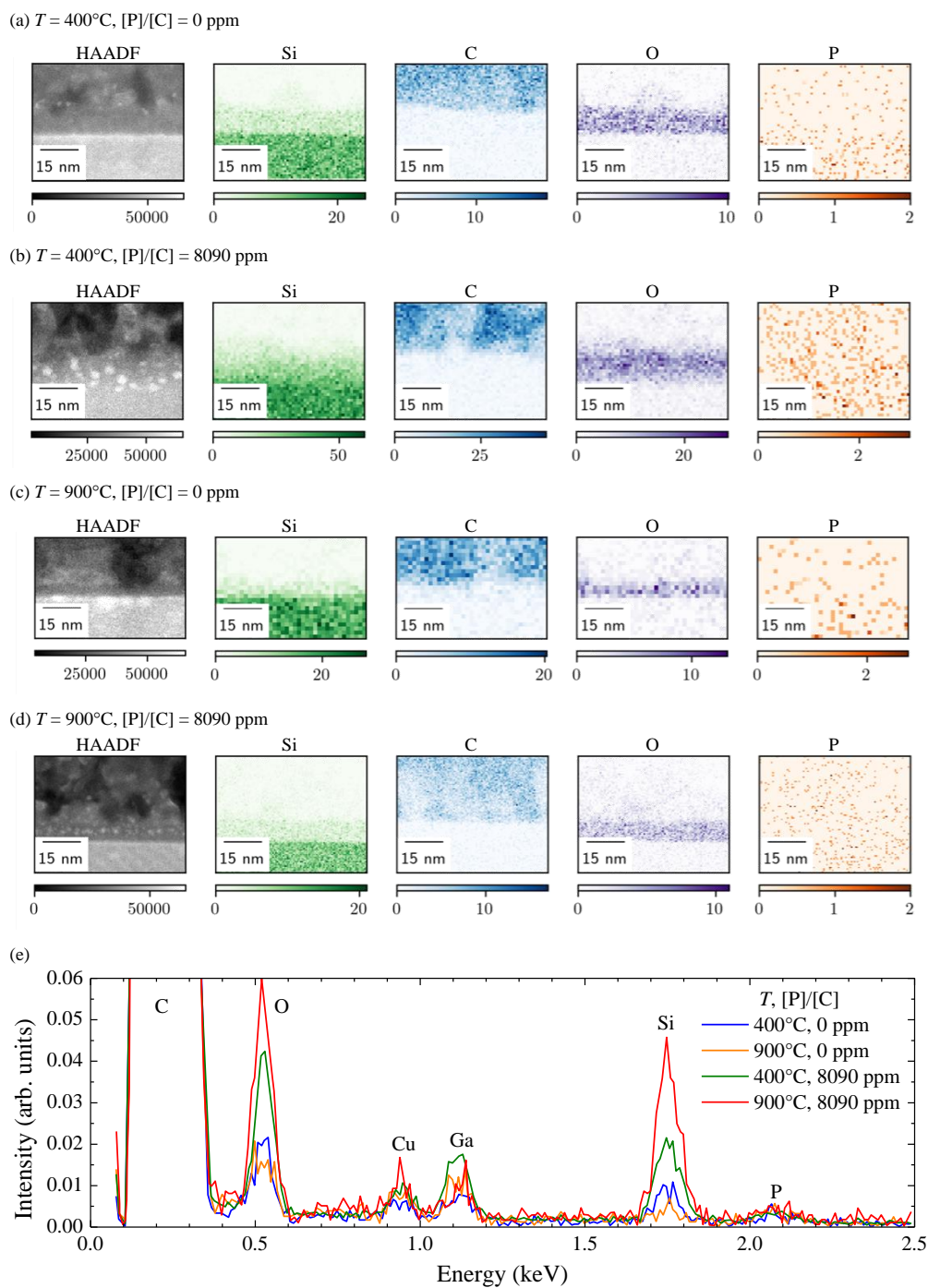


Figure S6: (a-d) High-angle annular dark-field imaging (HAADF) and EDX mapping. (e) Average EDX spectra of films deposited with $[\text{P}]/[\text{C}]$ ratio of 0 ppm and 8090 ppm at 400°C and 900°C . All spectra are normalized to the carbon X-ray peak.

References

- [1] P. Pobedinskas, G. Degutis, W. Dexters, J. D'Haen, M. Van Bael, K. Haenen, Nanodiamond seeding on plasma-treated tantalum thin films and the role of surface contamination, *Appl. Surf. Sci.* 538 (2021) 148016. doi:10.1016/j.apsusc.2020.148016.
- [2] F. De La Peña, E. Prestat, V. T. Fauske, P. Burdet, T. Furnival, P. Jokubauskas, M. Nord, T. Ostasevicius, J. Lähnemann, K. E. MacArthur, D. N. Johnstone, M. Sarahan, J. Taillon, T. Aarholt, P. Quinn-Dls, V. Migunov, A. Eljarrat, J. Caron, T. Poon, S. Mazzucco, B. Martineau, Suhas Somnath, T. Slater, C. Francis, Actions-User, M. Walls, N. Tappy, N. Cautaeerts, F. Winkler, G. Donval, *Hyperspy: Release v1.6.3* (2021). doi:10.5281/ZENODO.4923970.
- [3] A. Kromka, J. Breza, M. Kadlečiková, J. Janik, F. Balon, Identification of carbon phases and analysis of diamond/substrate interfaces by Raman spectroscopy, *Carbon* 43 (2) (2005) 425–429. doi:10.1016/j.carbon.2004.10.004.
- [4] M. Varga, T. Izak, V. Vretenar, H. Kozak, J. Holovsky, A. Artemenko, M. Hulman, V. Skakalova, D. S. Lee, A. Kromka, Diamond/carbon nanotube composites: Raman, FTIR and XPS spectroscopic studies, *Carbon* 111 (2017) 54–61. doi:10.1016/j.carbon.2016.09.064.
- [5] N. Wada, S. A. Solin, Raman efficiency measurements of graphite, *Physica B+C* 105 (1) (1981) 353–356. doi:10.1016/0378-4363(81)90274-6.
- [6] J. Wagner, C. Wild, P. Koidl, Resonance effects in Raman scattering from polycrystalline diamond films, *Appl. Phys. Lett.* 59 (7) (1991) 779–781. doi:10.1063/1.105340.
- [7] S. Drijkoningen, P. Pobedinskas, S. Korneychuk, A. Momot, Y. Balasubramaniam, M. K. Van Bael, S. Turner, J. Verbeeck, M. Nesládek, K. Haenen, On the origin of diamond plates deposited at low temperature, *Cryst. Growth Des.* 17 (8) (2017) 4306–4314. doi:10.1021/acs.cgd.7b00623.